Hybrid antireflection structure with moth eye and multilayer coating for organic photovoltaics

**Shigeru Kubota, Kensaku Kanomata,
Takahiko Suzuki, Bashir Ahmmad, Fumihiko Hirose**

Abstract We propose a hybrid antireflection structure (ARS), which integrates moth eye texturing and multilayer interference coating, to improve efficiency of organic photovoltaic (OPV) solar cells. We perform nearly global optimization of the geometric parameters characterizing the hybrid ARS, by using optical simulations based on the finite-difference time-domain method. The proposed optimization algorithm consists of two steps: in the first step, only the moth eye structure is globally optimized and, in the second step, the whole hybrid structure is optimized efficiently based on the results of the first step. Thus, the optimal moth eye structure is additionally obtained as an intermediate result. By applying this optimization method to an organic thin film solar cell, we show that the short-circuit current density (J_{SC}) is increased by 8.90% with the moth eye structure and by 9.89% with the hybrid ARS. We also study the sensitivity of photocurrent to the geometric parameters of hybrid ARS, and the change in the spatial distribution of electric field intensity by the ARS. The results show that the hybridization of the two types of light trapping techniques is effective to reduce the inhomogeneity in the electric field distribution and obtain higher electric intensity in almost the whole active layer. The design concept of the hybrid ARS is quite useful for improving light trapping in OPVs and allows for extending the options available for broadband antireflection.

Keywords Organic solar cell, Moth eye, Multilayer antireflection coating, Optimization, Optical simulation

S. Kubota (✉), K. Kanomata, T. Suzuki,
B. Ahmmad, F. Hirose
Graduate School of Science and Engineering, Yamagata University, 4-3-16 Jonan, Yonezawa, Yamagata 992-8510, Japan
e-mail: kubota@yz.yamagata-u.ac.jp

Introduction

Organic photovoltaics (OPVs) have been attracting considerable attention due to their potential for large-area, flexible, and low-cost solar cells.[1–4] The power conversion efficiency of OPVs has been rapidly increasing in the past decade,[5] although further improvement will be required for large-scale commercialization. A key factor limiting the efficiency of OPVs is a low mobility of charge carriers in the organic semiconductors.[6–8] To improve the carrier extraction from them, the thickness of the active layer, which is responsible for photocurrent generation, should be as small as ∼100 nm. To maximize the light absorption in such a thin active layer, it is particularly important to develop an efficient antireflection (AR) coating that allows for broadband light trapping.

The antireflection structure (ARS) is categorized to mainly two techniques, i.e., the single- or multilayer coating and surface texturing. Currently, the ARS that is most widely used is the multilayer interference structure, in which transparent materials with different refractive indexes are deposited in one dimension.[9] This simple structure can effectively reduce the mismatch in optical admittance to suppress reflection of light for a certain range of wavelength. To further improve the performance, recent studies are focusing on the ARS with moth eye texturing, in which the surface of a device is covered with two-dimensional array of cones which have the period and height of several hundred nanometers.[10–15] In a recent experimental study that applied moth eye structure to an OPV based on poly(3-hexylthiophene) (P3HT) and [6,6]-phenyl-C_{61}-butyric acid methyl ester (PCBM) blend, an increase in the performance by 2.5–3% was observed for a wide range of incident angles.[15]

Recent studies also suggest that the antireflective performance of moth eye structure significantly depends on the geometric feature of cone array.[11,14]

Boden and Bagnall[11] performed optical simulations for silicon moth eye array, and showed that the reflectance is given by a complicated function of the wavelength as well as the period and height of moth eye texturing. A theoretical study by Deinega et al.[14] also showed that, for silicon-textured surfaces, the minimum reflectance is achieved when each cone has sufficiently large height, and the period of moth eye array takes an optimal value within a very narrow range. These findings strongly suggest that the numerical optimization of geometric parameters is essential to bring out the full potential of moth eye structure. However, the global optimization of the textured pattern is quite difficult, because the optical simulation of three-dimensional nanostructure is generally computationally costly due to the necessity of fine division of space and time.[16] In addition, most previous simulation studies on the surface nanostructure are limited to the cases of silicon substrate, and therefore, the optimal configuration of the textured surface for OPVs is largely unclear.

When the moth eye texturing is applied to OPVs, it is additionally important that the textured material should have compatibility with the advantage of OPV devices, such as large-scale manufacturing. From this aspect, the use of organic polymers is highly beneficial, because the textured surface made of polymers can be easily fabricated by nanoimprint lithography (NIL) with polymeric resists.[17,18] In a wide range of applications, the technology of polymer NIL is used for a low-cost realization of a large-area nanopatterned surface.[19,20] However, the use of polymers for the front surface of organic solar cells produces another problem, that is, the discontinuity in the refractive index between the OPV itself and the surface structure. Since the discontinuous change in the reflective index inevitably produces reflection, it may be worth making use of multilayer interference coat, in addition to moth eye, to reduce such optical mismatching.

From these viewpoints, we consider numerical optimization of a novel hybrid ARS that integrates the moth eye and multilayer interference structures. We propose a nearly global optimization algorithm for the geometric parameters of the hybrid ARS. By the optical simulations based on the finite-difference time-domain (FDTD) method,[16] we demonstrate the effectiveness of the hybrid ARS in improving the short-circuit current density (J_{SC}) of OPVs. In addition, we investigate the sensitivity of J_{SC} to the characteristic parameters of the ARS, and show that the level of J_{SC} significantly depends on the period of moth eye array. Furthermore, we study the changes in the absorption spectrum and the electric field distribution by ARS, which underlie the enhancement in performance. The proposed hybrid ARS, combined with the quasi-global optimization method, provides a new option available for improving light trapping in the thin active layer of OPVs.

Experimental

Optical model

We numerically analyzed the optical properties of ARS by the FDTD simulations. Figure 1a shows a structure of the OPV cell in the absence of ARS, which serves as the reference for evaluating performance. In the OPV device, the thin films of P3HT:PCBM and MoO$_3$ work as the active layer and the hole transporting layer, respectively. These materials are sandwiched between the transparent forward electrode of the indium-doped tin oxide (ITO) and the bottom electrode of Al. Thus, the layer configuration of the OPV is summarized as ITO (100 nm)/MoO$_3$ (7 nm)/ P3HT:PCBM (100 nm)/Al (100 nm). The OPV device structure with the moth eye coat is illustrated in Fig. 1b, where the cones are hexagonally arranged on the front surface of the device. The base circles of two adjacent cones in the moth eye array touch each other. The configuration of moth eye structure is determined by the period L of the cone array and the height H of each cone. We assume that the moth eye structure is fabricated with organic polymer, because a large-scale nanostructure can be readily fabricated by NIL with polymeric resists,[17–20] as mentioned above. Accordingly, in our model, the refractive index of moth eye array is set to be 1.5, which is a typical value for polymer materials.[21] The device structure of the OPV with the hybrid ARS, proposed in this study, is given in Fig. 1c. The hybrid ARS contains the moth eye array and the two-layer coat composed of Al$_2$O$_3$ and MgF$_2$ films, in which the Al$_2$O$_3$ layer is deposited adjacent to the moth eye surface. Both Al$_2$O$_3$ and MgF$_2$ are the materials typically used for multilayer AR coating (e.g., reference 22). The thicknesses of the Al$_2$O$_3$ and MgF$_2$ films are denoted as d_1 and d_2, respectively.

Additionally, Fig. 1 implies that the examined structures have an inverted configuration,[23] in which the bottom Al electrode is in contact with the substrate. We consider the inverted structure, throughout this study, for the following two reasons. First, in the conventional devices, the existence of a very thick substrate at the front surface greatly increases the calculation time for FDTD simulations[24] and makes the numerical optimization extremely difficult (see below for the computation time). Second, due to the recent advancements in deposition techniques, several studies realized the room temperature deposition of high-quality ITO thin films, which allow for the inverted configuration.[25–27] In addition, obviously the proposed design method for hybrid ARS can be applied to improve the performance of the conventional OPV devices by using computers with higher computing power (e.g., supercomputer).

The coordinate system is defined as shown in Fig. 1. The incident light is assumed to propagate along z-direction. The absorbing boundary conditions with perfectly matched layer[16] are imposed for the upper
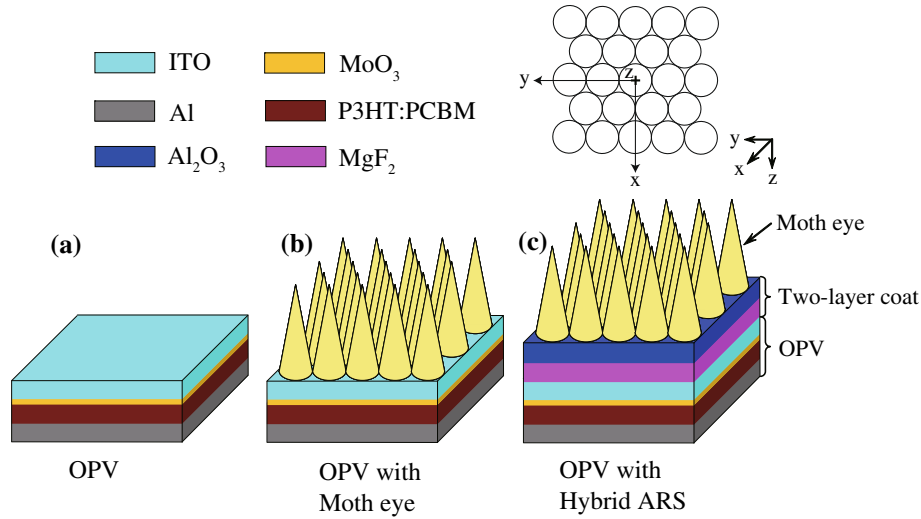
Fig. 1: Structures of a reference OPV cell (a), an OPV cell with only moth eye array (b), and an OPV cell with the proposed hybrid ARS (c) (Color figure online)

Table 1: Optimal parameters for the moth eye array and hybrid ARS, which are obtained by Steps 1 and 2 in the proposed algorithm, respectively

	Moth eye	Hybrid ARS
L (nm)	592	608
H (nm)	901	797
d_1 (nm)	0	186
d_2 (nm)	0	15
J_{SC} (mA/cm^2)	11.68 [8.90%]	11.78 [9.89%]

L and H are the period and height of moth eye array, respectively, and d_1 and d_2 are the thicknesses of the Al$_2$O$_3$ and MgF$_2$ films, respectively. The values in square brackets show the increase rate of J_{SC} compared to the reference cell

and lower boundaries in z-direction. The FDTD simulation using the inputs of unpolarized light, such as sunlight, usually requires the averaging of the results obtained with the x- and y-polarized light.[23] However, in the devices considered in this study (Fig. 1), due to a high symmetry of moth eye array, the difference in J_{SC} by using the x- and y-polarized incident light was much smaller than the change obtained by ARS (9–10%; Table 1). Therefore, we show the results obtained by the x-polarized incident light throughout this study.

To evaluate J_{SC}, the absorbance in the active layer was calculated for a range of wavelengths from 300 to 700 nm. To obtain the optical response for this range of wavelength in a single simulation, the results of FDTD simulation by a brief input pulse were Fourier transformed.[16] If we define $A_p(\lambda)$ to be the absorbance in the active layer at wavelength λ, the number of

photons absorbed in this layer, corresponding to λ, is described by the following equation[23,28]:

$$N_p(\lambda) = A_p(\lambda)F(\lambda)\frac{\lambda}{hc}. \tag{1}$$

Here $F(\lambda)$ represents the spectrum of solar irradiance under the AM 1.5 standard,[29] h is Planck's constant, and c is the speed of light in free space. With the unit charge q, the number of photons is converted into the generated photocurrent as follows[23,28]:

$$J_{SC} = \int_0^{\lambda_g} qN_p(\lambda)F_{NR}(\lambda)d\lambda, \tag{2}$$

where λ_g is the wavelength corresponding to the band gap energy of P3HT (653 nm). $F_{NR}(\lambda)$ is the nonrecombination factor, which is simply assumed to be 1 for all λ.[30] In addition, the weighted reflectance is obtained by the following equation[31]:

$$R_w = \frac{\int_0^{\lambda_g} R(\lambda)F(\lambda)d\lambda}{\int_0^{\lambda_g} F(\lambda)d\lambda}, \tag{3}$$

where $R(\lambda)$ is the reflectance at wavelength λ.

The optical data for the materials of MoO$_3$, P3HT:PCBM (1:1 by weight), Al, Al$_2$O$_3$, and MgF$_2$ were obtained by the measurements of spectroscopic ellipsometry for the range of wavelength of interest (300–700 nm). The optical data for ITO were taken from Hoppe et al.[32] These data were fitted by the Lorentz-Drude model,[33] which allows for efficient FDTD simulations for the dispersive materials.[16]

Optimization Algorithm

Numerical optimization of the parameters characterizing the hybrid ARS was conducted to maximize J_{SC}. There are four parameters to be optimized, i.e., the period L and height H of the moth eye array, and the thicknesses d_1 of the Al_2O_3 film and the thickness d_2 of the MgF_2 film. To efficiently obtain quasi-global optimal solution, we constructed a new algorithm that combines the simple grid search method[34,35] with the Hooke and Jeeves pattern search method.[34,36,37]

The simple grid search is an algorithm that is most frequently used for global optimization.[34,35] In this algorithm, a uniform grid is defined in the parameter space. Then, all the points in the grid are evaluated to find optimal solutions. In a parameter space spanned by N parameters x_i ($i = 1, …, N$), the grid is defined by selecting points for each coordinate $x_i^{(s)} = x_{i,min} + (s/n_i)$ $(x_{i,max} − x_{i,min})$ ($i = 1, …, N; s = 0, 1, …, n_i$). Here $[x_{i,min}, x_{i,max}]$ is the domain of parameter x_i, and n_i is the number of subdivisions of the domain. Thus, the total number of grid points is given as $\prod_{i=1}^{N}(n_i + 1)$. The local optimal solutions of the simple grid search are given, in this study, by the grid points in which J_{SC} is larger than that of any adjacent point in the grid.

The pattern search method proposed by Hooke and Jeeves[36] consists of iteration of two phases called exploratory and pattern moves. In the exploratory move, the search point travels in all the directions in the local parameter space near the base point $\mathbf{x}_b$, which is a starting point of the exploratory move. Let us define $\mathbf{x}_n$ to be a point that gives the best value of objective function among the points visited in the current exploratory move. In the pattern move which follows the exploratory move, the base point is shifted by a relatively long distance such that $\mathbf{x}_b ← \mathbf{x}_n + (\mathbf{x}_n − \mathbf{x}_p)$, where $\mathbf{x}_p$ is the point with the best objective function value obtained in the previous iteration.[34] The vector $\mathbf{x}_n − \mathbf{x}_p$ predicts the best search direction at the present time. The pattern move aims to accelerate the search based on the information about the objective function acquired in the past. The new base point is used for the exploratory move in the next round. The pattern search is terminated when the base point arrives at a local optimum, in which the exploratory move cannot improve the value of objective function.

The objective of the simple grid search is to obtain rough estimation of the global optimal solution, whereas the objective of the pattern search is to refine the solution obtained by the grid search. Therefore, the step size used in the pattern search ($\Delta L = 16$, $\Delta H = 1$, $\Delta d_1 = 1$, $\Delta d_2 = 1$) (in nm) is much smaller than that used in the grid search ($\Delta L = 96$, $\Delta H = 100$, $\Delta d_1 = 20$, $\Delta d_2 = 20$) (in nm) for each parameter.

The FDTD simulation of the present model takes time of the order of 10 min ($\sim$20–40 min) for each case, on our PC equipment (Intel Core i7 2.93 GHz). This high computational cost makes it extremely difficult to use common global optimization algorithms, which require more than thousands of times of function evaluation (e.g., reference 38). Therefore, to reduce the total computation time, we divide the optimization procedure into two steps. In the first step, we conduct global optimization only for L and H, by maintaining the values of d_1 and d_2 at 0, which means the optimization of moth eye array in absence of two-layer coat. This is because in our device model, the solar cell performance depends primarily on the characteristics of moth eye structure (see "Results and discussion"). In the second step, all the parameters for hybrid ARS are optimized by using the results of the first step as the starting point. By this two-step procedure, we can reduce the volume of search space that is actually relevant for each step, and can efficiently obtain quasi-global optimal solution which can be used for practical application.

The proposed optimization algorithm is described as follows:

Step 1. Optimization of moth eye structure.
Step 1-1. Perform the simple grid search with respect to L and H, by keeping the values of d_1 and d_2 at 0, and find the optimal solution.
Step 1-2. For the refinement of the solution, execute the pattern search with respect to L and H with maintaining $d_1 = d_2 = 0$. Here, the starting point for parameter set (L, H) is given by the solution of Step 1-1. Let us define (L^*, H^*) to be the optimal parameter set obtained by the pattern search.
Step 2. Optimization of the whole structure of hybrid ARS.
Step 2-1. Keep the values of L and H at those obtained by Step 1-2 (i.e., $L = L^*$ and $H = H^*$), and conduct the simple grid search with respect to d_1 and d_2. Let us denote the local optimal solutions of the parameter set (d_1, d_2) as $(d_{1,i}^*, d_{2,i}^*)$ (for $i = 1, …, M$), with the number of solutions M.
Step 2-2. Execute the pattern search M times to optimize all the parameters L, H, d_1, and d_2, by using each of the parameter set $(L^*, H^*, d_{1,i}^*, d_{2,i}^*)$ ($i = 1, …, M$) as the starting point. Then, as the final solution, select the best of the M solutions obtained by the pattern search.

Note that, in Step 1, we can obtain globally optimal structure of moth eye array as an intermediate result. The present simulation is performed by repetitively running the FDTD software, OptiFDTD, from a MATLAB program. Typically, the four-dimensional pattern search in Step 2-2 requires around 50–200 times of function evaluation, which corresponds to $\sim$25–100 h of computation time for the PC with Intel Core i7 2.93 GHz. We additionally carried out careful comparisons between the results of the FDTD method and those of the characteristic matrix method,[9] to ensure the stability and accuracy of our simulations.

Results and discussion

Optimization of hybrid ARS

We performed optimization of the hybrid ARS (Fig. 1 c), according to the two-step algorithm. In Step 1, we carried out global optimization of the period L and height H of moth eye array in absence of multilayer AR coat, i.e., $d_1 = d_2 = 0$. Figures 2a and 2b show the parameter-dependent change in the increase rate of J_{SC}, compared to the J_{SC} value of reference cell (Fig. 1a; $J_{SC} = 10.72$ mA/cm^2), which was obtained by the simple grid search in Step 1-1. As shown in the figures, only in a restricted region of parameter space ($L = \sim 600$ nm and 500 nm $< H < 1200$ nm), the increase rate of J_{SC} attains $>8\%$, while this value decreases abruptly in the neighborhood of this region. This finding indicates that the AR performance is quite sensitive to the geometric parameters of moth eye array near the optimal parameter region. The optimal solution obtained by the grid search was $L = 576$ nm and $H = 900$ nm (x-mark in Fig. 2a), which corre-

sponds to $J_{SC} = 11.64$ mA/cm^2 (i.e., 8.56% higher efficacy than the reference cell). The enhancement of J_{SC} was correlated negatively with the weighted reflectance (Fig. 2b), implying that the greater performance relies on the improved light trapping. The increase ratio of J_{SC} is as small as $\sim 2\%$ for $L < 400$ nm (Figs. 2a and 2b), although this range of L was typically used in previous studies.[39–41] The results here suggest that properly selecting the geometric parameters of moth eye is very important to fully bring out its potential to enhance light trapping in OPVs.

In order to refine the solution, we performed the pattern search[34,36,37] in Step 1-2, by setting the starting search point at the solution obtained by Step 1-1. We found the global optimal solution of moth eye array given as $L^* = 592$ nm and $H^* = 901$ nm. The corresponding value of J_{SC} was 11.68 mA/cm^2, which was 8.90% higher than the reference cell (Table 1).

In Step 2, we conducted optimization of all the parameters for hybrid ARS, by making use of the result of Step 1. The simple grid search was performed in Step 2-1 to optimize the parameters of d_1 and d_2,
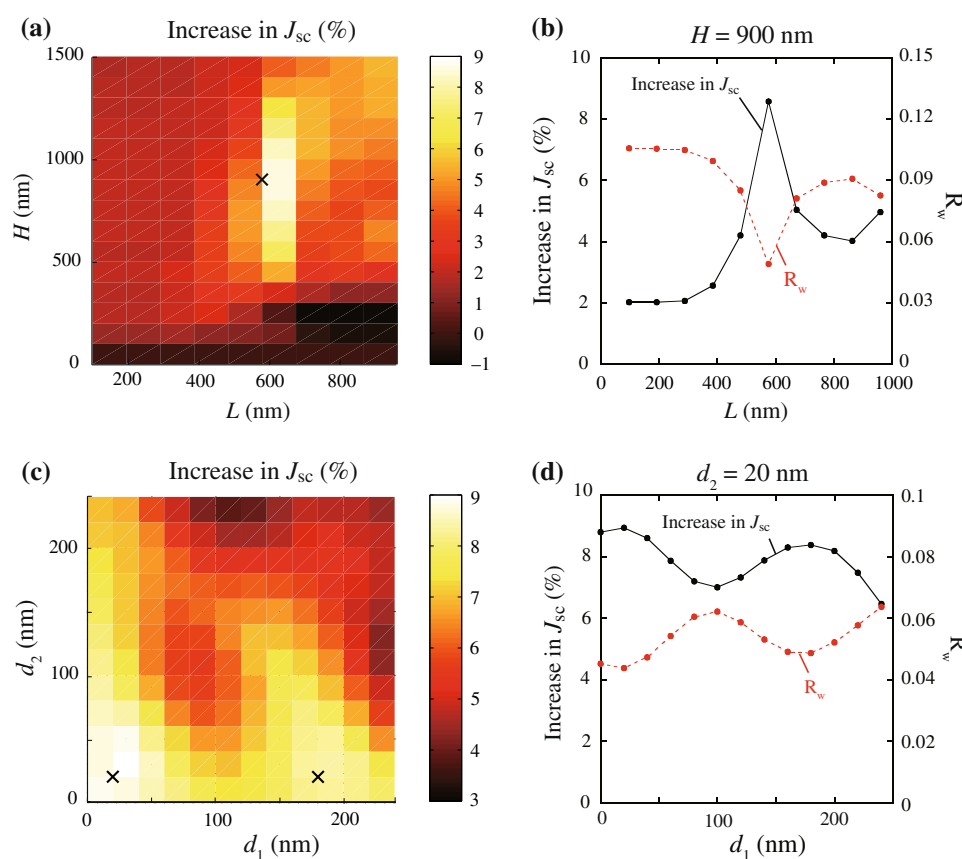

Fig. 2: Results obtained by the simple grid search in Step 1-1 (a, b) and Step 2-1 (c, d) in the proposed optimization algorithm. (a, c) The increase rate of J_{SC}, compared to that of the reference cell, is plotted as function of the period L and height H of moth eye array (a) or as function of the thickness of Al$_2$O$_3$ film, d_1, and the thickness of MgF$_2$ film, d_2 (c). The x-marks denote the points corresponding to the local maxima of J_{SC}, which are used for the starting points of the pattern search following the grid search. (b, d) The increase rate of J_{SC} (solid) and the weighted reflectance R_w (dashed) are plotted as function of L (b) and d_1 (d) ($H = 900$ nm in (b) and $d_2 = 20$ nm in (d))
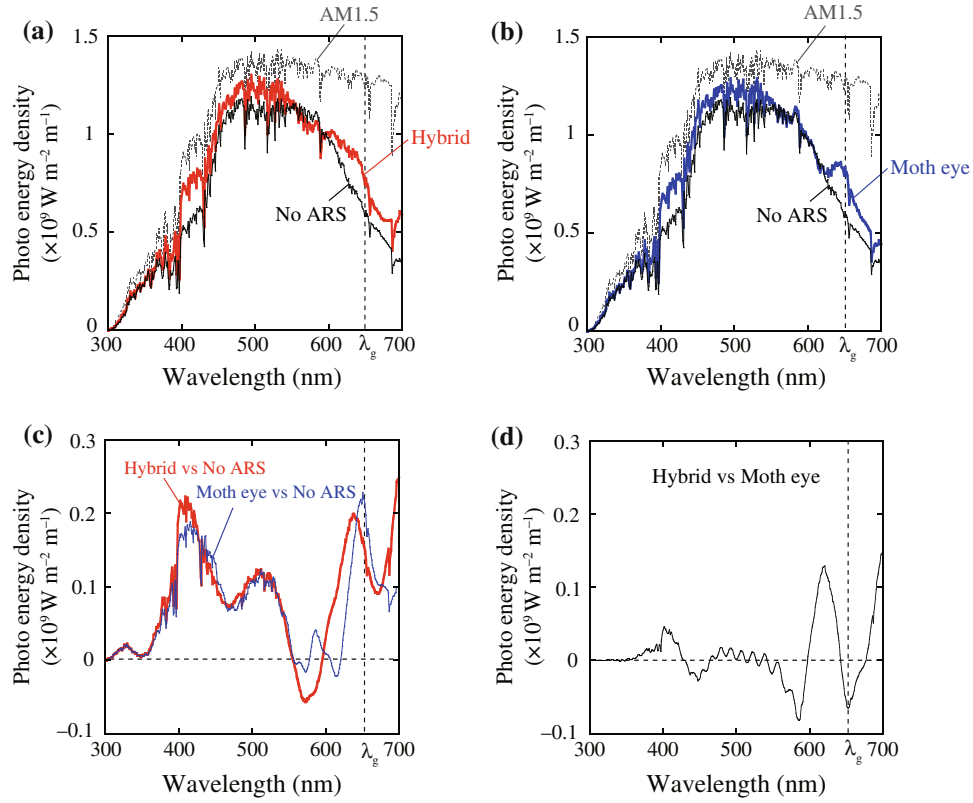
Fig. 3: Effects of applying the hybrid ARS and moth eye structure, with optimized configuration, on the spectrum of absorption energy in the active layer. (a, b) The absorption spectra in the active layer for the cases of using the optimized hybrid ARS (red) or the optimized moth eye structure (blue) and for the cases of not using ARS (black). The AM1.5 solar spectrum is shown with the gray dotted lines. (c) Red line: the difference in absorption spectra between the cases of using the hybrid ARS and not using ARS. Blue line: the difference in absorption spectra between the cases of using the moth eye and not using ARS. (d) The difference in absorption spectra between the cases of using the hybrid ARS and the moth eye array (Color figure online)

where L and H were fixed at the values of L^* and H^*, respectively. Figure 2c shows the increase rate of J_{SC}, due to the incorporation of ARS, as a function of d_1 and d_2. The figure indicates that there are mainly two subregions of parameter space in which J_{SC} is locally increased (i.e., the subregions with white colors surrounding the two x-marks). This is because the change in J_{SC} shows periodicity with respect to the thickness d_1 of the Al_2O_3 film (Fig. 2d), due to an interference effect of light passing through the thin film.[9] The level of J_{SC} alters gradually everywhere in the parameter space of d_1 and d_2. This finding is contrast to the fact that J_{SC} shows abrupt changes in the parameter space of L and H (Fig. 2a). As a result of the grid search, we found three local optimal solutions (i.e., $M = 3$): $(d_{1,1}^*, d_{2,1}^*) = (180, 20)$, $(d_{1,2}^*, d_{2,2}^*) = (20, 20)$, and $(d_{1,3}^*, d_{2,3}^*) = (0, 0)$ (in nm). The points of $(d_{1,1}^*, d_{2,1}^*)$ and $(d_{1,2}^*, d_{2,2}^*)$ are shown by the x-marks in Fig. 2c.

In Step 2-2, we conducted the pattern search with respect to all the four parameters L, H, d_1, and d_2. Here, the starting point was set as $(L, H, d_1, d_2) = (L^*, H^*, d_{1,1}^*, d_{2,1}^*)$ or $(L^*, H^*, d_{1,2}^*, d_{2,2}^*)$, which we refer to as the No. 1 or No. 2 parameter set, respectively. The starting point of $(L^*, H^*, d_{1,3}^*, d_{2,3}^*)$ was omitted, because this parameter set is obviously a local optimal solution, from the results of Step 1 and Step 2-1. The solutions obtained with the starting point of the No. 1 and No. 2 parameter set were $(L, H, d_1, d_2) = (608, 797, 186, 15)$ and $(576, 847, 19, 27)$ (in nm), which corresponded to the J_{SC} value of 11.78 and 11.75 mA/cm^2, respectively. These values of J_{SC} are higher than that of Step 1 ($J_{SC} = 11.68$ mA/cm^2). From the comparison among them, the solution obtained from the No. 1 parameter set gives the final optimal solution for the hybrid ARS, which produces 9.89% increase in J_{SC} (Table 1).

Optical properties of the optimized ARS

In the previous section, we obtained the optimal structures of both the moth eye array and hybrid ARS (Table 1). To elucidate the optical properties of the two types of ARS, we analyzed the wavelength-dependent change in light absorption. We plotted the spectra of absorption energy in the active layer of the

OPV with and without the optimized hybrid ARS (Fig. 3a, red and black, respectively) and the difference between these cases (Fig. 3c, red). The results show that the absorption energy is increased by applying the hybrid ARS for a wide range of wavelength λ for 300–700 nm, except for the narrow region of $\lambda \approx 570$ nm. Similarly, as shown in Fig. 3b (blue and black) and Fig. 3c (blue), the absorption in the active layer is
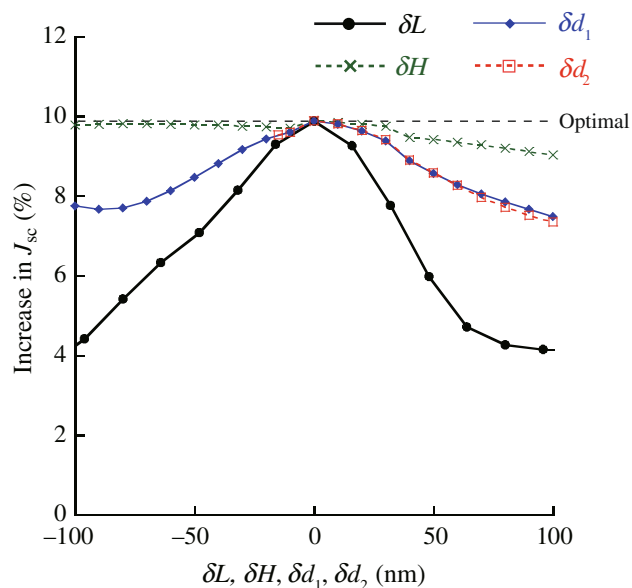
enhanced for a wide range of λ with the optimized moth eye structure. In Fig. 3d, we also compared the difference in the absorption spectra between the cases of applying the hybrid ARS and the moth eye array with the optimized parameters. The figure shows that the difference between them is particularly large at longer wavelengths for 600–650 nm. This result suggests that the hybridization of the moth eye and multilayer coating has a strong impact on the optical response at the longer wavelength near that of the band gap of P3HT (653 nm).

We also studied the sensitivity of the performance of hybrid ARS to the deviations in the characteristic parameters. Let us define δX ($X = L, H, d_1$, or d_2) to be the deviation of parameter X from its optimal value for the hybrid ARS in Table 1. Then, J_{SC} can be obtained by simulation for a given value of δX for the parameter X. In Fig. 4, we plotted the increase ratio of J_{SC}, compared to the reference cell, as a function of δL, δH, δd_1, and δd_2 using the same x-coordinate. From definition, the value of J_{SC} corresponding to $\delta X = 0$ gives the photocurrent density for the optimal solution. The figure clarifies that the deviation in L has the largest impact on the AR performance (Fig. 4, black), and the deviation of $\delta L = \pm 100$ nm decreases the antireflective effect to around 40% of the maximum level. On the other hand, the deviations in the other parameters have significantly smaller impact on the performance. The higher sensitivity of the AR performance to the period of moth eye array was also suggested by a recent study.[14]

To explore the reason for this remarkable effect of the L values on the performance, we studied how the absorption spectrum in the active layer depends on the deviation in L from its optimal value. We plotted the absorption spectra for the cases with and without

Fig. 4: Increase rate of J_{SC} by the hybrid ARS is shown as function of δL (black), δH (green), δd_1 (blue), and δd_2 (red), which represent the deviations of L, H, d_1, and d_2 from the optimal values (Table 1), respectively. The lower limit of δd_2 is set to be -15 nm because the optimal value of d_2 is 15 nm (Color figure online)
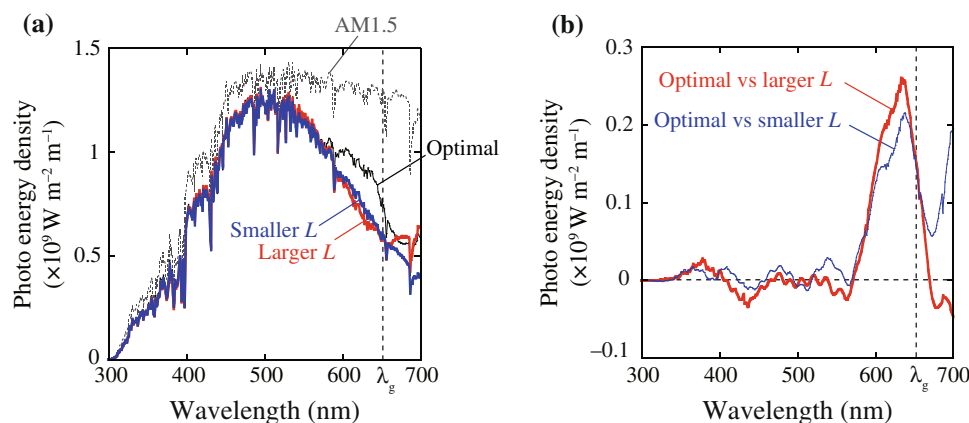
Fig. 5: Effects of changing the value of L in the hybrid ARS from its optimized value (608 nm) on the spectrum of absorption energy in the active layer. (a) Black line: the absorption spectrum obtained with the optimized hybrid ARS (the same as Fig. 3a, red line). Red and blue lines: the absorption spectra obtained with the hybrid ARS in which L is larger (red) or smaller (blue) than the optimal value by 96 nm. Gray dotted line: AM1.5 solar spectrum. (b) Red line: difference in the absorption spectra between the cases using the optimized hybrid ARS and the ARS with the larger L value. Blue line: difference in the absorption spectra between the cases using the optimized hybrid ARS and the ARS with the smaller L value (Color figure online)
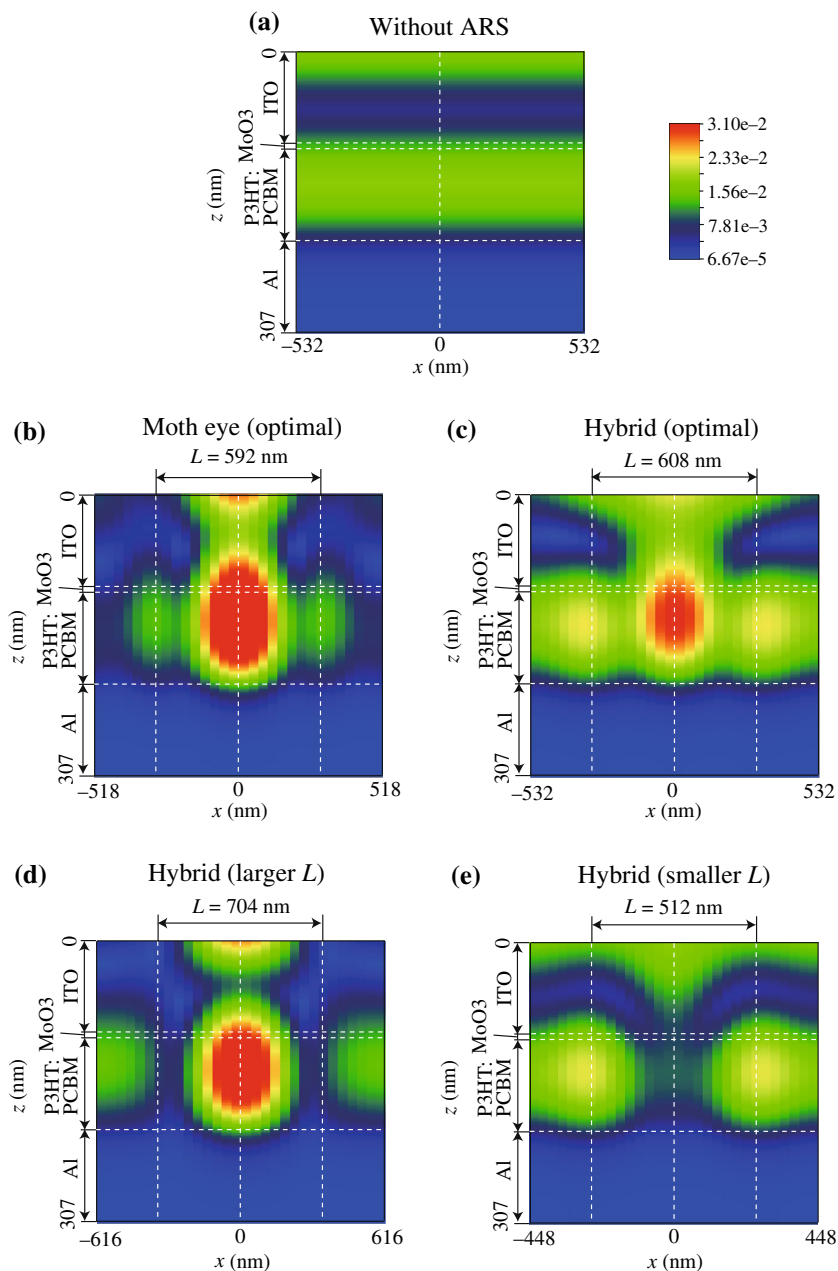
Fig. 6: Spatial distribution of electric field intensity in the OPV is shown at λ = 636 nm for the cases without ARS (a), with the optimized moth eye structure (b), with the optimized hybrid ARS (c), and with the hybrid ARS using the optimized parameters except for L (d, e). (d, e) The value of L is larger (d) or smaller (e) by 96 nm than the optimal value (608 nm). (a-e) The amplitude of the x-component of electric field is shown as function of x and z in the plane of $y = 0$ (see Fig. 1 for the coordinate system). The vertical line of $x = 0$ passes the center of the base circle of a cone in moth eye array, and the region denoted by horizontal two-headed arrows with length L ($-L/2 < x < L/2$) shows the region below the base circle. The distribution of the x-component of electric field is plotted, because the y-component of electric field disappears, due to a spatial symmetry of our model, and the z-component of electric field in the active layer tends to be much smaller than the x-component, due to the use of the x-polarized incident light (see "Experimental")

the deviation in L (Fig. 5a) and the difference between these cases (Fig. 5b). Here, we considered both the cases where L is larger and smaller than the optimal value (608 nm) by 96 nm (i.e., $\Delta L = \pm 96$ nm). The figures show a large change in absorption energy for a range of longer wavelength of $\lambda > 570$ nm. This range of wavelength nearly agrees with the L values considered here (608 $\pm$ 96 nm), implying the involvement of the diffraction effect caused by periodic surface.[42]

The results obtained so far indicate that the optical response at longer wavelengths, a little below the band gap of P3HT (653 nm), is particularly important to determine the performance of ARS (Figs. 3d and 5b). The absorption in the longer wavelength range is highly associated with the difference in the performance between the hybrid ARS and moth eye array (Fig. 3d), and also is responsible for the strong impact of L values on the performance of hybrid ARS (Fig. 5b). In order to clarify the light propagation in OPVs at this wavelength range, we plotted the spatial distribution of the electric field intensity at $\lambda = 636$ nm (Fig. 6). In absence of ARS (Fig. 6a), the electric field intensity changes across the layers, but is homogeneous in the horizontal direction (i.e., in the direction parallel to the layer interfaces), as expected. In contrast, the use of the optimized moth eye structure made the electric field inhomogeneous in the horizontal direction (Fig. 6b). As shown in the figure, within the active layer, the region with strong electric intensity is sandwiched by the regions with electric intensity which is weaker even than the level obtained in the active layer without ARS (Fig. 6a). Importantly, as shown in Fig. 6c, the use of the optimized hybrid ARS tended to flatten the electric field intensity and made more homogeneous distribution, compared to the case of using the moth eye only (Fig. 6b). In most of all the area of the active layer, the electric field obtained by the hybrid ARS (Fig. 6c) is maintained at a level that is significantly higher than that obtained without ARS (Fig. 6a). Furthermore, in cases where the period L of moth eye array was increased (Fig. 6d; $L = 704$ nm) or decreased (Fig. 6e; $L = 512$ nm) by 96 nm from the optimal value (608 nm) for the hybrid ARS, the homogeneity of the electric field was considerably lost and the subregions with very low electric intensity emerged. Therefore, the period of moth eye array plays an important role in regulating the level of homogeneity of the electric field distribution in the active layer. These results suggest that the excellent performance of the optimized hybrid ARS is attributable to the intensified electric field with higher homogeneity, which effectively makes use of almost the whole area of the active layer.

In the optical model of this study (Fig. 1), the moth eye texture is assumed to be a periodic array of precisely shaped cones, although this is an idealized model. From an experimental point of view, it is important to elucidate the effects of variations in textured pattern, which arise in fabrication processes, on the performance of solar cells. We evaluated the level of decrease in photocurrent due to the deviations in the geometric parameters of hybrid ARS from the optimal values (Fig. 4). However, it remains unclear how the antireflective effect of hybrid ARS can be affected by other types of variations such as the roundness at the tip and edge of cones or the spatial gap between adjacent cones.[43] It is a future work to study the effects of such variations in geometric characteristics of hybrid ARS on its performance and to design ARS which can improve solar cell efficiency even in the presence of this effect.

Conclusion

In this study, we considered light trapping of OPVs by the hybrid ARS that integrates moth eye array and multilayer interference coating. We proposed a two-step algorithm to find quasi-global optimal configuration of the hybrid ARS. In the first step of our algorithm, the moth eye structure was globally optimized in the absence of the multilayer coating. In the second step, the whole structure of hybrid ARS was optimized by using the solutions of the first step as the starting search point. In each step, the simple grid search and the pattern search were used for rough estimation of the optimal solution and for the refinement of the solution, respectively. The increase ratio of J_{SC} by the optimal moth eye structure and hybrid ARS were 8.90% and 9.89%, respectively (Table 1).

We also investigated the spectrum of absorption energy in the active layer, and showed that the optical response at longer wavelengths, a little lower than that of the band gap of P3HT (653 nm), is quite important to determine the difference in AR performance between the moth eye structure and hybrid ARS (Fig. 3d). We additionally showed that the deviation in the period of moth eye array from the optimal value has a strong impact on the performance by decreasing absorption at the longer wavelength range (Figs. 4 and 5b). Furthermore, we studied the spatial distribution of electric field intensity at the longer wavelength and showed that the optimized hybrid ARS contributes to maintaining the electric field in almost the whole active layer at higher level (Fig. 6c). These results show the effectiveness of the hybrid ARS for improving light trapping in the thin active layer of OPVs. By adjusting the materials used in the multilayer interference coating, the hybrid structure with the same concept will also be applicable to light trapping of other thin film solar cells.

References

1. Yu, G, Gao, J, Hemmelen, JC, Wudl, F, Heeger, AJ, "Polymer Photovoltaic Cells: Enhanced Efficiencies Via a Network of Internal Donor–Acceptor Heterojunctions." *Science*, **270** 1789–1791 (1995)
2. Sariciftci, NS, Smilowitz, L, Heeger, AJ, Wudl, F, "Photo-induced Electron Transfer from a Conducting Polymer to Buckminsterfullerene." *Science*, **258** 1474–1476 (1992)

3. Park, SH, Roy, A, Beaupre, S, Cho, S, Coates, N, Moon, JS, Moses, D, Leclerc, M, Lee, K, Heeger, AJ, "Bulk Heterojunction Solar Cells with Internal Quantum Efficiency Approaching 100%." *Nat. Photonics*, **3** 297–303 (2009)

4. Krebs, FC, Espinosa, N, Hösel, M, Sondergaard, RR, Jorgensen, M, "25th Anniversary Article: Rise to Power—OPV-Based Solar Parks." *Adv. Mater.*, **26** 29–39 (2014)

5. Jorgensen, M, Norrmann, K, Cevorgyan, SA, Tromholt, T, Andreasen, B, Krebs, FC, "Stability of polymer Solar Cells." *Adv. Mater.*, **24** 580–612 (2012)

6. Niggemann, M, Blasi, B, Gombert, A, Hinsch, A, Hoppe, H, Lalanne, P, Meissner, D, Wittwer, V, "Trapping Light in Organic Plastic Solar Cells with Integrated Diffraction Gratings." *Proc. 17th Eur. Photovoltaic Solar Energy Conf.*, Munich, Germany, 2001

7. Niggemann, M, Riede, M, Gombert, A, Leo, K, "Light Trapping in Organic Solar Cells." *Phys. Status Solidi A*, **205** 2862–2874 (2008)

8. Raman, A, Yu, Z, Fan, S, "Dielectric Nanostructures for Broadband Light Trapping in Organic Solar Cells." *Opt. Express*, **19** 19015–19026 (2011)

9. Macleod, HA, *Thin-Film Optical Filters*, 4th ed. CRC Press, Boca Raton, 2010

10. Brunner, R, Sandfuchs, O, Pacholski, C, Morhard, C, Spatz, J, "Lessons From Nature: Biomimetic Subwavelength Structures for High-Performance Optics." *Laser Photonics Rev.*, **6** 641–659 (2012)

11. Boden, SA, Bagnall, DM, "Optimization of Moth-Eye Antireflection Schemes for Silicon Solar Cells." *Prog. Photovolt. Res. Appl.*, **18** 195–203 (2010)

12. Sun, CH, Jiang, P, Jiang, B, "Broadband Moth-Eye Antireflection Coatings on Silicon." *Appl. Phys. Lett.*, **92** 061112 (2008)

13. Huang, YF, Chattopadhyay, S, "Nanostructure Surface Design for Broadband and Angle-Independent Antireflection." *J. Nanophotonics*, **7** 073594 (2013)

14. Deinega, A, Valuev, I, Potapkin, B, Lozovik, Y, "Minimizing Light Reflection from Dielectric Textured Surfaces." *J. Opt. Soc. Am. A*, **28** 770–777 (2011)

15. Forberich, K, Dennler, G, Scharber, MC, Hingerl, K, Fromherz, T, Brabec, CJ, "Performance Improvement of Organic Solar Cells with Moth Eye Anti-Reflection Coating." *Thin Solid Films*, **516** 7167–7170 (2008)

16. Taflove, A, Hagness, SC, *Computational Electrodynamics: The Finite-Difference Time-Domain Method*. Artech House Inc., Norwood, 2005

17. Han, KS, Shin, JH, Yoon, WY, Lee, H, "Enhanced Performance of Solar Cells with Anti-reflection Layer Fabricated by Nano-imprint Lithography." *Sol. Energy Mater. Sol. Cells*, **95** 288–291 (2011)

18. Jiao, F, Huang, Q, Ren, W, Zhou, W, Qi, F, Zheng, Y, Xie, J, "Enhanced Performance for Solar Cells with Moth-Eye Structure Fabricated by UV Nanoimprint Lithography." *Microelectron. Eng.*, **103** 126–130 (2013)

19. Boltasseva, A, "Plasmonic Components Fabrication Via Nanoimprint." *J. Opt. A*, **11** 114001 (2009)

20. Brigo, L, Mattei, G, Michieli, N, Brusatin, G, "2D Photonic Gratings from Thermal Imprinting of ITO-Based Films." *Microelectron. Eng.*, **97** 193–196 (2012)

21. Lü, C, Yang, B, "High Refractive Index Organic–Inorganic Nanocomposites: Design, Synthesis and Application." *J. Mater. Chem.*, **19** 2884–2901 (2009)

22. Bouhafs, D, Moussi, A, Chikouche, A, Ruiz, JM, "Design and Simulation of Antireflection Coating Systems for Optoelectronic Devices: Application to Silicon Solar Cells." *Sol. Energy Mater. Sol. Cells*, **52** 79–93 (1998)

23. Ren, W, Zhang, G, Wu, Y, Ding, H, Shen, Q, Zhang, K, Li, J, Pan, N, Wang, X, "Broadband Absorption Enhancement Achieved by Optical Layer Mediated Plasmonic Solar Cell." *Opt. Express*, **19** 26536–26550 (2011)

24. Wang, J, Wang, CW, Li, Y, Zhou, F, Liu, WM, "The Structure Optimization Design of the Organic Solar Cells Using the FDTD Method." *Physica B*, **405** 2061–2064 (2010)

25. Farhan, MS, Zalnezhad, E, Bushroa, AR, Sarhan, AAD, "Electrical and Optical Properties of Indium–Tin Oxide (ITO) Films by Ion-Assisted Deposition (IAD) at Room Temperature." *Int. J. Precis. Eng. Manuf.*, **14** 1465–1469 (2013)

26. Kurdesau, F, Khripunov, G, da Cunha, AF, Kaelin, M, Tiwari, AN, "Comparative Study of ITO Layers Deposited by DC and RF Magnetron Sputtering at Room Temperature." *J. Non Cryst. Solids*, **352** 1466–1470 (2006)

27. Xiao, Y, Gao, F, Dong, G, Guo, T, Liu, Q, Ye, D, Diao, X, "Amorphous Indium Tin Oxide Films Deposited on Flexible Substrates by Facing Target Sputtering at Room Temperature." *Thin Solid Films*, **556** 155–159 (2014)

28. Kubota, S, Kanomata, K, Momiyama, K, Suzuki, T, Hirose, F, "Robust Design Method of Multilayer Antireflection Coating for Organic Solar Cells." *IEICE Trans. Electron.*, **96** 604–611 (2013)

29. ASTM G173-03, "Standard Tables for Reference Solar Spectral Irradiances," ASTM International, West Conshohocken, 2005

30. Darkwi, AY, Lote, WK, Ibrahim, K, "Computer Simulation of Collection Efficiency of a—Si:H Tandem Solar Cells Interconnected by Transparent Conductive Oxide." *Sol. Energy Mater. Sol. Cells*, **60** 1–9 (2000)

31. Luk, WC, Yeung, KM, Tam, KC, Ng, KL, Kwok, KC, Kwong, CY, Ng, AMC, Djurisic, AB, "Enhanced Conversion Efficacy of Polymeric Photovoltaic Cell by Nanostructured Antireflection Coating." *Org. Electron.*, **12** 557–561 (2011)

32. Hoppe, H, Sariciftci, NS, Meissner, D, "Optical Constants of Conjugated Polymer/Fullerene Based Bulk-Heterojunction Organic Solar Cells." *Mol. Cryst. Liq. Cryst.*, **385** 113–119 (2002)

33. Rakic, AD, Djurisic, AB, Elazar, JM, Majewski, ML, "Optical Properties of Metallic Films for Vertical-Cavity Optoelectronic Devices." *Appl. Opt.*, **37** 5271–5283 (1998)

34. Dixon, LCW, *Nonlinear Optimization*. The English Universities Press, London, 1972

35. Momma, M, Bennett, KP, "A Pattern Search Method for Model Selection of Support Vector Regression." *Proc. SIAM Conf. Data Mining*, Philadelphia, 2012

36. Hooke, R, Jeeves, TA, "Direct Search Solution of Numerical and Statistical Problems." *J. Assoc. Comput. Mach.*, **8** 212–229 (1961)

37. Khambampati, AK, Ijaz, UZ, Lee, JS, Kim, S, Kim, KY, "Phase Boundary Estimation in Electrical Impedance Tomography Using the Hooke and Jeeves Pattern Search Method." *Meas. Sci. Technol.*, **21** 035501 (2010)

38. Yi, H, Duan, Q, Liao, TW, "Three Improved Hybrid Metaheuristic Algorithms for Engineering Design Optimization." *Appl. Soft Comput.*, **13** 2433–2444 (2013)

39. Raut, HK, Dinachali, SS, He, AY, Ganesh, VA, Saifullah, MSM, Law, J, Ramakrishna, S, "Robust and Durable Polyhedral Oligomeric Silsesquioxane-Based Anti-reflective Nanostructures with Broadband Quasi-omnidirectional Properties." *Energy Environ. Sci.*, **6** 1929–1937 (2013)

40. Lee, SW, Han, KS, Shin, JH, Hwang, SY, Lee, H, "Fabrication of Highly Transparent Self-cleaning Protection Films

for Photovoltaic Systems." *Prog. Photovolt. Res. Appl.*, **21** 1056–1062 (2013)

41. Tommila, J, Aho, A, Tukiainen, A, Polojärvi, V, Salmi, J, Niemi, T, Guina, M, "Moth-Eye Antireflection Coating Fabricated by Nanoimprint Lithography on 1 eV Dilute Nitride Solar Cell." *Prog. Photovolt. Res. Appl.*, **21** 1158–1162 (2013)

42. Born, M, Wolf, E, *Principles of Optics*, 7th ed. Cambridge University Press, Cambridge, 1999

43. Ji, S, Song, K, Nguyen, TB, Kim, N, Lim, H, "Optimal Moth Eye Nanostructure Array on Transparent Glass Towards Broadband Antireflection." *ACS Appl. Mater. Inter.*, **5** 10731–10737 (2013)